

1 **Statistical Study of the Non-thermal Continuum Radiation Beaming Angle measured**  
2 **by the High Frequency Receiver on Van Allen Probes-A**

3  
4 **S. A. Boardsen<sup>1,2</sup>, E.-H. Kim<sup>3</sup>, J. L. Green<sup>4</sup>, C. Z. Cheng<sup>3</sup>, I. H. Cairns<sup>5</sup>, J. R. Johnson<sup>6</sup>**

5 <sup>1</sup>NASA Goddard Space Flight Center, Greenbelt, Maryland, USA.

6 <sup>2</sup>Goddard Planetary Heliophysics Institute, University of Maryland in Baltimore, Maryland,  
7 USA.

8 <sup>3</sup>Princeton Plasma Physics Laboratory, Princeton University, Princeton, New Jersey, USA

9 <sup>4</sup>Space Science Endeavors LLC, Silver Spring, Maryland, USA

10 <sup>5</sup>Department of Physics, University of Sydney, Sydney, New South Wales, Australia

11 <sup>6</sup>Department of Engineering, Andrews University, Berrien Springs, Michigan, USA

12

13 Corresponding author: S. A. Boardsen ([scott.a.boardsen@nasa.gov](mailto:scott.a.boardsen@nasa.gov))

14

15 **Key Points:** (140 characters or less with no special characters or acronyms)

- 16 • Nonthermal continuum radiation beaming angles are calculated over the entire seven-year  
17 mission of Van Allen Probes-A.

18       • For frequencies  $\lesssim 100$  kHz the observed beaming angle pattern is consistent with the  
19       predictions from linear mode conversion theory.

20       • For frequencies  $\gtrsim 100$  kHz another mechanism along with linear mode conversion is  
21       needed.

22

23   **Keywords:** Linear Mode Conversion Theory, Nonthermal Continuum Radiation, Terrestrial  
24   Myriametric Radiation

25

26

**27 Abstract**

28 The nonthermal continuum radiation (NTC) beaming angle is computed over the entire Van  
29 Allen Probes A mission when the spacecraft was in the dawn sector. The conditions in the dawn  
30 sector are favorable for the wave vector to lie near/in the spacecraft's spin plan allowing a  
31 favorable estimate of the beaming angle, and the dawn sector is also advantageous in that  
32 previous studies show NTC occurrence to peak in this sector. We found that scatter plots, over  
33 the entire mission, of beaming angle versus magnetic latitude form a distinct inverted-V pattern,  
34 with the apex at/near the magnetic equator. This pattern was sharpest for frequencies ( $f$ )  $\lesssim$  100  
35 kHz. Using the NTC beaming formula from the linear mode conversion theory (LMCT), we  
36 show that such an inverted-V pattern is expected due to the large variation in the plasmopause  
37 location over the entire mission. The theoretical derived pattern qualitatively reproduces the  
38 observed pattern but not quantitatively. The lack of quantitative agreement is discussed and is  
39 attributed to several factors, one factor is off-centered emissions from the radio window. The  
40 qualitative agreement strongly supports LMCT as being the dominant mechanism generating  
41 NTC for  $f \lesssim$  100 kHz. For  $f \gtrsim$  100 kHz the inverted-V pattern becomes less distinct, and strong  
42 near-equatorial beaming is observed. After considering contamination of our selections by left-  
43 handed polarized AKR, our study suggests that besides LMCT another unidentified NTC  
44 generation mechanism becomes important for  $f \gtrsim$  100 kHz.

45

**46 Plain Language Summary**

47 No summary given. Not required.

## 48 1. Introduction

49 Non-thermal continuum (NTC) radiation (also called terrestrial myriametric radiation) is  
50 free space ( $f > f_{pe}$ , where  $f$  and  $f_{pe}$  are the wave and plasma frequencies respectively)  
51 electromagnetic (EM) radiation for waves in the left-handed ordinary (L-O) mode observed in  
52 and near the Earth's magnetosphere and mainly outside the plasmasphere (Gurnett & Shaw,  
53 1973; Gurnett 1975). NTC is believed to be emitted at strong density gradients chiefly at the  
54 equatorial plasmopause and is associated with electrostatic (ES) waves near the upper hybrid  
55 frequency (Gough et al., 1979; Kurth et al., 1981) and electron injections (Gough, 1982). This  
56 radiation can be produced over a broad frequency range from ~10 kHz to 100's of kHz and is  
57 roughly divided into two categories 1) trapped continuum where  $f < f_{pe}$  at the magnetopause and  
58 escaping continuum where  $f > f_{pe}$  at the magnetopause (Kurth et al., 1981). For  $f \gtrsim 100$  kHz,  
59 escaping radiation is often called kilometric continuum (KC) radiation (Hashimoto et al., 1999;  
60 Green et al., 2002; Green et al., 2004; Hashimoto et al., 2005).

61  
62 The widely accepted theory for the generation of NTC is linear mode conversion theory  
63 (LMCT) (Jones, 1976; Budden, 1980; Horne et al., 1989; Kim et al., 2013, Schleyer et al., 2014).  
64 In this theory electrostatic waves (ES) at frequencies of  $\sim(n+1/2)f_{ce}$  (Kurth et al., 1979), where  $f_{ce}$   
65 is the electron cyclotron frequency, are generated by electron loss cone distributions (Gough et  
66 al., 1979; Rönmark & Christiansen, 1981) or weak ring-like features in the electron distribution  
67 (Sentman et al., 1979; Kurth et al., 1980) at/near the magnetic equator. As these ES waves  
68 propagate toward the higher density plasmopause, they convert into EM Z-mode waves on the  
69 same dispersion branch (e.g., Oya, 1971). Mode conversion from incoming Z-mode to the free  
70 space L-O wave mode radiation occurs at the radio window, where the Z-mode frequency

71 matches the local electron plasma frequency. This process is depicted in Figure 4 of Jones (1980)  
 72 and Figure 8 of Horne et al. (1989).

73

74

75 The key prediction of LMCT by Jones (1976) is that the mode-converted L-O mode  
 76 waves can form two symmetrical beams relative to the magnetic equator as they propagate away  
 77 from the equatorial plasmapause into lower densities outside the plasmasphere. The LMCT  
 78 beaming formula is.

$$79 \quad \theta_B = \tan^{-1} \sqrt{\frac{f_{pe\_w}}{f_{ce\_w}}}. \quad (1)$$

80 Here,  $\theta_B$  is the beaming angle measured from the background magnetic field at the radio window  
 81  $\mathbf{B}$  ( $\mathbf{k} \parallel +\mathbf{B}$ ) or  $-\mathbf{B}$  ( $\mathbf{k} \parallel -\mathbf{B}$ ),  $\mathbf{k}$  is a wave vector,  $f_{pe\_w}$  and  $f_{ce\_w}$  are the electron plasma and cyclotron  
 82 frequencies at the window, respectively, and at the radio window,  $f = f_{pe\_w}$  (Jones, 1980). The  
 83 beaming formula holds at the window center where the waves experience no attenuation upon  
 84 crossing. The window center is where the incoming Z-mode  $\mathbf{k}$  is either parallel or anti-parallel to  
 85  $\mathbf{B}$ . Therefore, if Z-mode waves are propagating into the window from both the  $+\mathbf{B}$  and  $-\mathbf{B}$   
 86 directions, two symmetric L-O mode free space beams about the magnetic equator will be  
 87 emitted from the radio window. We note that  $\theta_B$  is the predicted asymptotic refraction  
 88 (propagating away from the radio window as the index of refraction  $\rightarrow 1$ ) of  $\mathbf{k}$  away from the  $\mathbf{B}$   
 89 direction as it propagates into the lower plasma density. For a typical plasmapause density  
 90 gradient, this refraction of  $\mathbf{k}$  from  $\theta$  of  $0^\circ$  at the radio window center to  $\sim \theta_B$  will occur over a  
 91 radial distance of less than  $\sim 0.1 R_E$ , where  $R_E$  is Earth's radii (Jones, 1980; Horne, 1989). For  
 92 off-centered emission's the wave attenuation increases as the deviation of the beaming angle

93 away from  $\theta_B$  increases (Budden, 1980). We note that studies often use the complement of  $\theta_B$ ;  
94  $\lambda_B = \tan^{-1}(\sqrt{f_{ce_w} / f_{pe_w}})$ , which is a beaming angle between  $\mathbf{k}$  and the magnetic equatorial plane.

95

96 The acceptance of the LMCT theory is based primarily on Jones et al. (1987), where  
97 Dynamics Explorer-1 observed two symmetrical NTC beams in magnetic latitude ( $\lambda_M$ ) as the  
98 spacecraft transverses the magnetic equator. Other follow-up studies seeking to further verify the  
99 LMCT interpretation have either negative or mixed results (Morgan & Gurnett, 1991; Grimald et  
100 al., 2007) on the beaming angle predictions. Two multi-event/case studies of KC using  
101 GEOTAIL (Hashimoto et al., 2005) and IMAGE (Boardsen et al., 2008) spacecraft concluded  
102 that the LMCT beaming formula predicted too small (too large if complement of beam angle is  
103 used instead) of a beam angle  $\theta_B$  compared to the  $\lambda_M$  where the KC was observed.

104

105 In this paper, using the Van Allen Probes-A High Frequency Receiver (HFR) dataset over  
106 the entire mission, we perform a statistical study of the observed beaming angle  $\theta_B$  as a function  
107 of the spacecraft position and compare it with that predicted by LMCT. This paper is organized  
108 as follows. Section 2 describes the dataset and how  $\theta_B$  is computed. Section 3 explores the  
109 statistical set of  $\theta_B$  observations. Section 4 derives the theoretically predicted beaming angle  
110 using equation (1) as a function of satellite location, followed by a discussion and conclusion.

111

## 112 **2. Remote Measurement of the Observed Beaming Angle**

113

114 For observational studies cited in the introduction and this study, the electromagnetic  
115 radiation in the NTC frequency range was only sampled by one spin plane electric field antenna.

116 Therefore, the only approach to estimate the wave vector direction and the source beaming angle  
 117 is from the analysis of the antenna's spin modulation curve. The modulation curve is (e.g., Kurth  
 118 et al., 1975)

119

$$120 \left(\frac{E_i}{E_0}\right)^2 = \left(1 - \frac{m}{2}\right) - \frac{m}{2} \cos[2(\delta_i - \delta)], \quad (2)$$

121

122 where  $E_i$  is the component of the vector electric field  $\mathbf{E}$  measured by the spacecraft antenna at  
 123 time step  $i$ ,  $E_0$  is the peak spin plane electric field,  $m$  is the modulation index,  $\delta$  is the azimuthal  
 124 angle of  $\mathbf{k}$  in the spin plane, and  $\delta_i$  is the antenna angle in the spin plane. At the time of the null  
 125 ( $\delta_i = \delta$ ) the antenna is aligned with the projection of  $\mathbf{k}$  onto the spin plane because  $\mathbf{k} \cdot \mathbf{E} = 0$  for free  
 126 space radiation. The modulation index  $m=1$  corresponds to full modulation ( $\mathbf{k}$  lies in the spin  
 127 plane) and  $m=0$  corresponds to no modulation.

128

129 In this study, we use the High Frequency Receiver (HFR) on the Van Allen Probes A  
 130 spacecraft (Kletzing et al., 2013) for which only one spin plane electric field antenna is sampled  
 131 by the receiver for a given time interval. Because we want  $\mathbf{k}$  to lie nearly in the spin plane to  
 132 estimate  $\theta_B$ , we need to analyze time intervals where the spin axis direction is nearly  
 133 perpendicular to the radial direction of the Earth. The Van Allen Probes spin axis vector, which  
 134 points to within  $\pm 28^\circ$  of the Sun, is nearly perpendicular to the radial direction for MLTs around  
 135 6 MLT and 18 MLT. Continuum typically peaks around dawn (Gurnett & Frank, 1976). Fits  
 136 were made only for periods when the angle between the spin axis and the radial position vector  
 137 (Earth centered) was within  $\pm 15^\circ$  of perpendicular orientation. In all, 6408 dawn sector time  
 138 intervals were processed from 2012/10/15 to 2019/06/20. The onboard HFR spectral

139 measurements consist of 82 logarithmically spaced frequencies ranging from 10 to 487 kHz. The  
 140 cadence of the frequency sweeps is 0.5 s, which is small compared to the spin period of ~11 s.  
 141 For each dawn sector time interval, spin modulation curve fits were performed on the HFR  
 142 spectra dataset (Kletzing et al., 2022). Fits were performed for each frequency over a time range  
 143 covering 1&1/2 spin periods (~33 measurements, ~17 s), staggering each time step by the one-  
 144 time measurement between individual fits. We note that other approaches could had been  
 145 performed like Fourier analysis over multiple spin periods of the spin modulation curve (Kurth et  
 146 al., 1975).

147 The analysis approach used in this study is that described in Morgan & Gurnett (1991).

148 We rewrite the modulation equation (2) as

$$149 \quad \rho_i(f) = C_1 + C_2 \cos(2\delta_i) + C_3 \sin(2\delta_i) \quad (3)$$

150 where  $\rho_i(f)$  is the measured electric field power spectral density at frequency  $f$ ,  $\delta_i$  is the antenna  
 151 spin phase angle at time step  $i$ , respectively, and  $C_1$ ,  $C_2$ , and  $C_3$  are the fit coefficients. Least  
 152 squares fit of equation (3) are made over all data points within  $\pm 3/4$  of a spin period about the time  
 153 of the center point  $i$ , solving for the fit coefficients  $C_1$ ,  $C_2$ , and  $C_3$ . A five-point smoothing is  
 154 performed on  $\rho_i(f)$  before fitting. The smoothing was performed to reduce the noise in the data,  
 155 however smoothing complicates the meaning of modulation index discussed later in this section.  
 156 The uncertainties of the fit coefficients  $\Delta C_1$ ,  $\Delta C_2$ , and  $\Delta C_3$  are computed from the product of their  
 157 variance with the diagonal elements of the covariance matrix (Bevington & Robinson, 1992). We  
 158 found that the off-diagonal elements of this matrix are small relative to the diagonal elements, so  
 159 the cross-correlations are set to zero when estimating the uncertainties in  $m$ ,  $\delta$ , and  $\lambda_0$ .

160



161 From  $C_1$ ,  $C_2$ ,  $C_3$ ,  $\Delta C_1$ ,  $\Delta C_2$ , and  $\Delta C_3$ , one can compute  $m$ ,  $\delta$ ,  $\lambda_0$ , and their uncertainties

162  $\Delta m$ ,  $\Delta \delta$ ,  $\Delta \lambda_0$  as

163

$$164 \quad m = 2\sqrt{C_2^2 + C_3^2} / \left( C_1 + \sqrt{C_2^2 + C_3^2} \right) \quad (4)$$

165

$$166 \quad \delta = \frac{1}{2} \tan^{-1}(C_3/C_2), \quad (5)$$

167

$$168 \quad \cos^2(\lambda_0) = m. \quad (6)$$

169

170 In equation (6)  $\lambda_0$  is the angle of  $\mathbf{k}$  out of the spin plane. The uncertainties  $\Delta m$ ,  $\Delta \delta$ ,  $\Delta \lambda_0$  are

171 computed from square root of the square of differential form of equations (4-6) and setting the

172 terms involving  $\Delta C_1 \Delta C_2$ ,  $\Delta C_2 \Delta C_3$ , and  $\Delta C_3 \Delta C_1$ , to zero due to their small cross-correlations. We

173 note that Fainberg (1979) uses a different representation of the modulation curve  $\left(\frac{E_i}{E_1}\right)^2 = 1 -$

174  $m' \cos[2(\delta_i - \delta)]$ , where  $E_1$  is a constant and  $0 \leq m' \leq 1$  is the modulation index, compared to

175 equation (1) of this paper. The relation between the modulation index's is  $m' = \frac{m}{2-m}$ ,  $\lambda_0$  would be

176 given by  $\cos^2(\lambda_0) = \frac{2m'}{1+m'}$ . Both approaches are equally valid. The representation by Fainberg

177 (1979) was used by Menietti et al. (1998) to estimate the direction of Jovian radio emissions.

178

179 Figure 1 is an example spin fit of the modulation curve for the frequency channel at 38.3

180 kHz. The fit parameters and their uncertainties are listed in the figure. For this fit, the uncertainty

181 in  $\delta$  is  $3.6^\circ$ , in 0.5 s between spectral measurements the antenna rotates through angle of  $\sim 16^\circ$ .

182 Using the spacecraft ephemeris (see Data Availability Statement) and the NAIF SPICE toolkit  
 183 (Acton, 1996; Acton et al. 2017), the antenna orientation at the time of the null in modulation  
 184 curve indicated by the blue curve in Figure 1 was computed. The antenna's unit vectors are in  
 185 Solar Magnetic (SM) coordinates ( $\mathbf{u}$ ,  $\mathbf{v}$ ,  $\mathbf{w}$ ), where  $\mathbf{u}$  and  $\mathbf{v}$  are in the spin plane, and  $\mathbf{w}$  is along  
 186 the spin axis. For SM coordinates, the origin is Earth centered and the Z-axis ( $Z_{SM}$ ) is parallel to  
 187 the north magnetic pole. If the HFR is connected to  $\mathbf{u}$  (or  $\mathbf{v}$ ) antenna, then projection of  
 188 wavevector  $\mathbf{k}$  into the spin plane ( $\hat{\mathbf{k}}_{sp}$ ) is aligned with  $\mathbf{u}$  (or  $\mathbf{v}$ ) to within a sign. The sign is  
 189 chosen such that  $-\mathbf{k}$  points Earthward (directed nearest to the  $Z_{SM}$  axis). The beaming angle  $\theta_B$  is  
 190 estimated as an angle between  $\hat{\mathbf{k}}_{sp}$  and  $Z_{SM}$  if the spacecraft is in the northern hemisphere, and  
 191  $\hat{\mathbf{k}}_{sp}$  and the  $-Z_{SM}$  axis if the spacecraft is in the southern hemisphere.

192

193 We retain only  $\theta_B$  measurements for which a plasma density measurement (Kurth et al.,  
 194 2015) was available in the plasma density data set (Kurth et al., 2020) for each fit time interval.  
 195 The local plasma density is needed to compute the local plasma frequency  $f_{pe}$  to restrict the  
 196 frequencies to the free space mode.

197

198 The 6408 processed time intervals were filtered for NTC emissions with strong  
 199 modulation using the following criteria:  $f > 1.2f_{pe}$ ,  $m > 0.6$ ,  $\Delta m/m < 0.2$ ,  $\chi^2/\chi_0^2 < 0.25$ . We use  
 200  $\chi^2/\chi_0^2 < 0.25$  in order that the sinusoidal fit is substantially improved over the constant offset fit  
 201 (where the fit curve is a constant) given by  $\chi_0^2$ . We also removed data during intervals judged to  
 202 be saturated, this removed about 4% of the data points. Applying this filter reduces our set of  $\theta_B$   
 203 measurements to  $1.6 \times 10^7$  frequency-time pixels. We found that the modulation index of type III

204 radio bursts was consistently  $< 0.4$ , so contamination of our selections by these radio bursts is  
 205 minimal.

206

207 Smoothing the signal will lower the modulation index because the dc component of the  
 208 signal will not change, while the ac component will become smaller in amplitude. If the signal is  
 209 a sine curve, the effect on  $m$  due to smoothing can be computed. The amplitude of a smoothed  
 210 sine curve of unit amplitude is given by.

211

$$212 \quad b(\alpha, n) = (1 + 2 \sin(n\alpha) \cos((n + 1)\alpha) / \sin(\alpha)) / (2n + 1), \quad (7)$$

213

214 where  $2n+1$  is the amount of smoothing, and  $\alpha$  is the angular increment between measurements.  
 215 For five-point smoothing  $n = 2$  and from the antenna rotation angle between measurements  $\alpha =$   
 216  $2 \cdot 16^\circ$ ,  $b(\alpha, n) = 0.715$ . The relation between  $m$  from the smooth sine curve and the modulation  
 217 index  $m_c$  from the non-smoothed sine curve is.

218

$$219 \quad m_c = 2m / (2b(\alpha, n) + m(1 - b(\alpha, n))). \quad (8)$$

220

221 The value  $m = 0.6$  used as the lower limit in filtering the data gives  $m_c = 0.750$ , which from  
 222 equation (6) gives an out of spin plane angle estimate limit of  $30^\circ$  for the wave vector.

223

224 Frequency-time spectrograms of two orbital segments where the spin modulation curves  
 225 were fitted are shown in Figures 2 and 3 for (a) spectral power density, (b) the modulation index  
 226  $m$ , (c) the chi-squared ratios  $\chi^2/\chi_0^2$  and (d) selections that satisfied the selection criteria. The red

227 line in Figure 2(d) at 53.6 kHz between 4.5 and 5  $R_E$  are data points used in Figures 8, 9, and 10.  
228 For  $f > 100$  kHz strong contamination of the selections can occur. Figure 3 shows an extreme  
229 example of selected emissions  $200 < f < 500$  kHz interpreted to be heavily contaminated by L-O  
230 mode AKR when the spacecraft is at  $\lambda_M > 10^\circ$  and  $R > 5.3 R_E$  in dawn sector (MLT  $\sim 6$ ). Green  
231 et al. (1977) using ray tracing showed that L-O mode can propagate from the source (dusk sector  
232 auroral field lines) across the polar cap and down to  $\lambda_M$  of about  $10^\circ$  on the dawn sector (unlike  
233 R-X mode AKR (Green et al., 1977; Xiao et al., 2016) which can easily propagate to the dusk  
234 sector equatorial inner magnetosphere). Looking at the ray tracing results of Green et al. (1977)  
235 this contamination will decrease as the magnetic latitude decreases in the dawn sector.

236

237         Histograms of the selected frequency-time pixels are presented in Figure 4 of (a) the radial  
238 distance ( $R$ ), (b)  $\lambda_M$  for  $f < 100$  kHz, (c) the magnetic local time (MLT), and (d)  $\lambda_M$  for  $f > 100$  kHz.  
239 The y-axis is the number of selected frequency-time pixels per bin. Splitting the frequencies into  
240 those below and those above 100 kHz is because the emissions show a distinct change in the spatial  
241 characteristics as discussed in the next section. The magnetic latitude histograms are substantially  
242 different between  $f < 100$  kHz (Figure 4(b)) and  $f > 100$  kHz (Figure 4(d)). While the lower  
243 frequency case ( $f < 100$  kHz) shows a deep minimum (notch like feature) at the magnetic equator,  
244 the higher frequency case ( $f > 100$  kHz) shows a strong peak at the magnetic equator. The former  $f$   
245  $< 100$  kHz is quantitatively consistent with LMCT in the sense that the beaming is predicted to be  
246 directed out of the equatorial plane, while the later  $f > 100$  kHz is not consistent with LMCT and  
247 is more consistent with the findings of Hashimoto et al. (2005) and Boardsen et al. (2008) where  
248 stronger equatorial beaming was suggested than that predicted by LMCT. The counts pick up  
249 moving away from the magnetic equator for  $f > 100$  kHz in Figure 4(d), and we interpret this to be

250 due to contamination of selections by L-O mode AKR which is predicted to become stronger as  
251  $\lambda_M$  increases (Green et al. 1977).

252

253

### 254 **3. Observed Beaming Angles Versus Magnetic Latitude**

255

256 We explored scatter plots of the selections for each frequency as a function of various  
257 parameters against beaming angle (e.g., radial distance, magnetic latitude, etc.). For scatter plots  
258 of magnetic latitude, the scatter exhibited an inverted-V pattern with the apex at/near the magnetic,  
259 with the pattern clearer for frequencies below 100 kHz. Figure 5 shows scatter plots of  $\theta_B$  versus  
260  $\lambda_M$  when spacecraft is located at a radial distance between 4 and 5  $R_E$  ( $4R_E < r < 5R_E$ ) for various  
261 frequency ranges, for a)  $f > 19$  and  $< 51$  kHz and b)  $f > 51$  kHz and  $f < 100$  kHz, c)  $f > 100$  kHz  
262 and  $f < 147$  kHz, and d)  $f > 147$  kHz and  $f < 500$  kHz. Beyond the division at 100 kHz, the choice  
263 of frequency boundaries is arbitrary. For Figure 5(a) and (c), a distinct statistical inverted-V pattern  
264 is observed about the magnetic equator. Note that the gap in detections in Figure 5(a) is consistent  
265 with the notch in the histogram in Figure 4(a). For Figure 5(b) and (d), an inverted-V signature for  
266  $|\lambda_M| < 10^\circ$  is observed in the running median, while for  $|\lambda_M| > 10^\circ$  we interpret the scatter to be  
267 strongly contaminated by L-O mode AKR.

268

269 Scatter plots of  $\theta_B$  versus MLAT for  $5.5 R_E < r < 6 R_E$  are shown in Figure 6(a-d). For the  
270 lower frequency radiations ( $f < 100$ kHz), an inverted-V pattern is observed about the magnetic  
271 equator as shown in Figure 6(a-b), while no inverted-V pattern is discernable for the higher  
272 frequencies as shown in Figure 6(b, d), which is interpreted to be due to L-O mode AKR

273 contamination. Can the inverted-V structure of beaming angles versus magnetic latitude observed  
274 in scatter plots covering the entire seven-year mission be explained in terms on LMCT? This will  
275 be explored in the next section.

#### 276 **4. Model Beaming Angle versus Spacecraft Position for Varying Plasmopause Location**

277 If LMCT is the principal generation mechanism, what is the predicted statistical  $\theta_B$  pattern as a  
278 function of spacecraft position and detected NTC frequency  $f$  for a wide range of plasmopause  
279 locations? Figure 7(a) illustrates the meridian geometry used to interpret the results of our  
280 observational data analysis. To connect the source with the observation: we assume straight-line  
281 motion of the radiation once it leaves the source region at the asymptotic beaming angle. This  
282 means that we ignore refraction along the path between the source region and the observer. There  
283 are many observational studies that use this assumption (e.g., Jones, 1987, Morgan & Gurnett,  
284 1991; Grimald et al., 2007). Based on the comparison with the observations in this study it appears  
285 that this assumption is reasonable. Because of this assumption no density model is needed, if one  
286 was going to ray trace from the radio window, yes both a plasma density and magnetic field model  
287 are needed, but this is not a ray tracing study. The ray tracing (e.g., Jones 1980, Jones 1981, Horn,  
288 1989) using a reasonable density model shows a straight-line ray path for the emitted free-space  
289 mode with a beaming angle near the asymptotic radio window beaming angle. However, a future  
290 paper using ray tracing under various density profiles quantifying the effects of refraction should  
291 be made.

292

293 The following assumptions are used: background magnetic field is an Earth center dipole anti-  
294 aligned with the  $Z_{SM}$  axis; the radio window is located at the equatorial plasmopause; the  
295 plasmopause is assumed to have local azimuthal symmetry; the emission is from the center of the

296 window. Under these assumptions, the ray lies in the meridian plane. In Figure 7(a), the radio  
 297 window ( $W$ ) is located at an equatorial plasmopause at  $2.5R_E$ , the blue line is the emitted NTC ray  
 298 path for  $f = f_{pe_w}$  from  $W$  to the spacecraft ( $SC$ ). Knowing the location of the radio window and  
 299 spacecraft the beaming angle can be computed as

$$300 \quad \tan \theta_B = \frac{\rho_{sc} - \rho_w}{z_{sc}}. \quad (9)$$

301 The  $SC$  and  $W$  locations in the  $\rho$  - $z$  plane is given by  $(\rho_{sc}, z_{sc})$  and  $(\rho_w, 0)$  respectively, where

302  $\rho = \sqrt{x^2 + y^2}$  in units of  $R_E$ . Using an Earth centered magnetic dipole  $f_{ce_w}$  is given as

$$303 \quad f_{ce_w} = \frac{870}{\rho_w^3} \text{ Hz} \quad (10)$$

304 for a dipole moment of  $3.11 \times 10^{-5}$  T. For this example, from the  $SC$  and  $W$  location  $\theta_B = 47.9^\circ$   
 305 from equation (9) and from equation (1&10)  $f = f_{pe_w} = 68.1$  kHz. For variable  $W$  location in  
 306 equatorial radius (Figure 7b) and fixed  $f$  and  $SC$   $r$  the solution of equations (1&9&10) results in  
 307 an inverted-V pattern for  $\theta_B$  versus  $\lambda_M$  (Figure 7c). The 4 dots in Figure 7(b) would be the beaming  
 308 values at 4 different frequencies if a sharp plasmopause was at 2.5 RE. The plasmopause could  
 309 span 1 frequency only, 2 adjacent frequencies, etc., at different radial locations, giving various  
 310 density profiles. As the plasmopause moves inwards or outwards from orbit to orbit under various  
 311 geomagnetic conditions the pattern in Figure 7(c) would be traced out.

312

313

314 Figure 7(b) shows how  $\theta_B$  varies for different source locations  $W$  in the equatorial radial  
 315 distance for four different NTC waves of  $f = 33.2, 53.6, 68.1,$  and  $121.0$  kHz. For example, for a  
 316 sharp plasmopause at  $2.5R_E$ ,  $\theta_B$  is equal to  $37.7^\circ, 44.4^\circ, 47.9^\circ$  and  $55.7^\circ$  for the four frequencies,  
 317 indicated by the black dots in Figure 7(b) and the latitudes at which the *SC* will observe them in  
 318 Figure 7(c). The increase in  $\theta_B$  with increasing  $\rho_{SM}$  in Figure 7(b) is due to the increasing  
 319  $f_{pe_w}/f_{ce_w}$  ratio with increasing  $\rho_{SM}$  for fixed  $f_{pe_w}$ . Thus, as the magnetosphere becomes less  
 320 active the geomagnetic  $K_p$  index decreases and the plasmopause moves outwards (e.g., Carpenter  
 321 & Anderson, 1992; Moldwin et al., 2002) and  $\theta_B$  will increase.

322 Figure 7(c) presents the predicted model  $\theta_B$  for an *SC* radial position at  $4.75 R_E$  as a function of  
 323 magnetic latitude  $\lambda_M$  for plasmopause locations varying between  $1.5$  to  $4.75 R_E$ . For a sharp  
 324 plasmopause at  $2.5R_E$ , the frequencies emitted at  $W$  (black dots in Figure 7(b) will be detected by  
 325 the *SC* with a radial position  $R_{SC} = 4.75R_E$  at  $\lambda_M = \pm 27.7^\circ, \pm 23.5^\circ, \pm 21.5^\circ,$  and  $\pm 17.0^\circ$  (black  
 326 dots in Figure 7c) for these four  $f$  respectively. For fixed radial position  $R_{SC}$  of the *SC*, as the  
 327 plasmopause location varies due to changing geomagnetic conditions, an inverted-V pattern of  
 328  $\theta_B$  versus  $\lambda_M$  with the apex located at the magnetic equator will be traced out as shown in Figure  
 329 7(c). The source location coincides with the virtual spacecraft position at the apex of the  
 330 inverted-V at  $\lambda_M \rightarrow 0^\circ$ . As noted, because the beaming formula is asymptotic  $\theta_B$  does not equal  
 331 the Z-mode angle of  $0^\circ$  at the radio window center.

332

333 Figure 8 shows a comparison of the observations with the model of Figure 7, for the same  
 334  $f$  and *SC* radial distances that lie within  $4.5 < r < 5 R_E$ . A scatter plot of  $\theta_B$  versus  $\lambda_M$  is shown in  
 335 Figures 8(a-d) for these four  $f$ . The error bars for  $\theta_B$  are plotted for 10 randomly selected points.  
 336 To restrict the wave vector to lie closer to the spin plane, only points are plotted for which  $m >$



337 0.8 ( $m_c = 0.96$ ). The three blue curves are the theory curves for SC positions at  $r$  of 4.5, 4.75, and  
 338  $5 R_E$ . Comparing the observations with the blue theory curves, one can see that the observations  
 339 are qualitatively consistent with the model but are not always quantitatively consistent. With the  
 340 disagreement of observed  $\theta_B$  with model the largest around  $\lambda_M$  of  $0^\circ$ , with the observations about  
 341  $10^\circ$  larger than the model  $\theta_B$ . Why quantitative agreement within measurement error is difficult  
 342 and maybe impossible to obtain is discussed in the next section.

343

344 For  $f = 33.2, 53.6,$  and  $68.1$  kHz a gap in the observations is observed straddling  $\lambda_M$  of  $0^\circ$   
 345 which would be expected from the off-equatorial beaming predicted by the theory. No such gap  
 346 is observed for the large clustering of points for  $f = 120$  kHz which is not consistent with the  
 347 theory. However, the lack of a gap could be due to by radiation produced by a second  
 348 mechanism.

349

350 Can we detect a  $K_p$  dependence related to changing plasmopause location over the entire  
 351 mission mentioned earlier in this section? Figure 8(e-h) plots  $K_p$  (Papitashvili & King, 2020)  
 352 versus  $\lambda_M$  for the selections of Figure 8(a-d). The red lines are linear fits for  $1 \leq K_p \leq 4$ , and the  
 353 number in each panel is the Spearman correlation coefficient. Unlike the linear fit, which is just a  
 354 visual aid, this correlation is a nonlinear correlation which measures the degree that the data is  
 355 monotonically related, a value of 1 indicates a strict monotonic increasing dependence, while a  
 356 value of -1 indicates a strict monotonic decreasing dependence. The negative sign of the  
 357 coefficients is consistent with the expected change in plasmopause position with  $\theta_B$ . However,  
 358 the correlation is weak for  $f = 33.2$  kHz with a value of -0.29, moderate for  $f = 53.6$  and  $68.1$  kHz  
 359 with values of -0.43 and -0.51 respectively, and for  $f = 120$  kHz the value of -0.21 is poor. So

360 below 100 kHz the correlation is moderate at best. We note that in the study of Moldwin et al.  
361 (2002) the non-linear correlation for the overall dataset of radial plasmopause position versus  $K_p$   
362 is 0.55 (see Figure 4 of that study), we should not expect to get a better correlation than this  
363 value since  $K_p$  is a not a perfect indicator of the plasmopause location. The uncertainty in the  
364 measurement of  $\theta_B$  will also degrade the correlation.

365

## 366 **5. Discussion**

367

368 Qualitatively the observations for  $f < 100$  kHz reproduce the inverted-V structure of  $\theta_B$   
369 vs.  $\lambda_M$  predicted by LMCT theory for the large variation in plasmopause location over the  
370 duration of the mission. However, the error bars of many measurements do not encompass the  
371 model curve, with a systematic bias, especially for observations near the magnetic equator. We  
372 discuss why one might not expect quantitative agreement. Three major simplifications are used  
373 in our analysis: 1) the dawn sector plasmopause in our model is azimuthally symmetric, it has no  
374 azimuthal dependence. This allows one to use the simple model shown in Figure 7 for  
375 comparison with data. 2) The out of spin plane component is not used in the computation of  $\theta_B$ ,  
376 we justify this by using only data points with a large modulation index  $m > 0.6$ . 3) The emissions  
377 not from the center of the radio window need to be considered.

378

379 A radially directed plasmopause gradient used in this study is obviously an  
380 approximation. There are azimuthal variations in the plasmopause location as observed by the  
381 Extreme Ultraviolet Imager on the IMAGE spacecraft (e.g., Sandel et al., 2003). Here we make a  
382 back of the envelope estimate of how this could lead to a systematic offset of about  $10^\circ$ . To

383 simplify the argument the measurement of azimuthal angles in SM coordinate system is shifted  
384 to the SC location. From Section 2, the lower limit used in the filter for the modulation index is  
385  $m=0.8$  ( $m_c = 0.96$ ) which after correcting for smoothing gives a maximum out of plane angle for  
386  $\mathbf{k}$  of about  $10.7^\circ$ . Combining this angle with the requirement that the analyzed data segments are  
387 within  $\pm 15^\circ$  of being radially directed gives an azimuthal angular range of  $\pm 26^\circ$ . So, if the source  
388 is not radially outwards, but directed  $26^\circ$  in azimuth from the radial direction, the radial location  
389 of the azimuthally directed radio window of the source can be estimated. If the spacecraft is near  
390 the equator at a radial distance is  $4.75 R_E$  and the plasmopause is  $2.5 R_E$  (for a radially directed  
391 outward beam), using the law of cosines a radial distance of about  $2.7 R_E$  for the radio window is  
392 computed for the azimuthally directed beam. Looking at Figure 7(b) the model beaming angle  
393 for a window at  $3 R_E$  is about 5 degrees larger than the beaming angle for a window at  $2.5 R_E$  and  
394 this will lead to a systematic offset. We note that the magnitude of the systematic offset will  
395 diminish as the radially directed window moves outward in radius, because the slope of the curve  
396 in Figure 7(b) decreases with increasing radius.

397

398 In principle, the modulation index  $m$  can be used to estimate the out of spin plane  
399 component of the wave vector direction. However, there are several factors that limit the  
400 interpretation of  $m$  and, therefore, its use in computing the out of spin plane component. 1) One  
401 factor is the variation of Z-mode radiation at the source over the time interval  $\sim 17$  s of the fit. For  
402 example, the detected NTC in Figure 1 is not sinusoidal, and this could be due to variation of the  
403 Z-mode radiation at the source. The deviation of the observations from a sinusoidal curve limits  
404 the interpretation of  $m$ . 2) The smoothing of the data will lower the estimate of  $m$ , but this can  
405 somewhat be overcome by using the estimated correction given by equation (8). 3) The presence

406 of background radiation can also degrade that interpretation of  $m$ , leading to a lowering of its  
 407 actual value.

408

409 Many observations of NTC are not emissions from near the window center where the  
 410 signal attenuation is near zero, but off centered where the signal experiences stronger  
 411 attenuation. We will address attenuation using the  $f=53.6$  kHz emissions from the orbit segment  
 412 shown in Figure 2. The attenuation equation (23) of Budden (1980) will be used. This equation  
 413 requires as input  $f_{ce_w}$ ,  $f=f_{pe_w}$ ,  $S_1$ ,  $S_2$  and  $G$ ; where  $S_1$  is the asymptotic direction cosine of the  
 414 emitted radiation along  $\mathbf{B}$ ,  $S_2=0$  is the direction cosine normal to both  $\mathbf{B}$  and the density gradient,  
 415 here  $\mathbf{B}$  is taken to be perpendicular to the density gradient, and the scalar of the density gradient  
 416 is  $G$ . To estimate the location of the window we will use the nearest plasmopause (Figure 9(a))  
 417 where  $f$  intersects  $f_{pe_w}$ , this occurs at 2016-07-12T18:37:06.482Z (red dots), where  $L=3.65$ ,  $|\lambda_M$   
 418  $= 7.18^\circ$ ,  $MLT=7$  h and  $f_{ce} = 18.34$  kHz. Projecting this location using a dipole field line to the  
 419 magnetic equator gives  $f_{ce_w}=17.04$  kHz. The density variation is assumed to be a function of  
 420 only L-shell, and  $G$  is estimated to be  $-1971 \text{ m}^{-4}$  from the gradient of the observed density  
 421 variation with L-shell (Figure 9(b)).

422

423 The radiation pattern from the radio window is shown in Figure 9(c),  $-10$  dB corresponds  
 424 to a decade decrease in power spectral density. The window center is indicated by the black dot  
 425 where the attenuation is 0 dB (100% transmission) and  $\phi$  is azimuthal angle measured from the  
 426 window location, a  $\phi$  of  $0^\circ$  is directed outwards. We note that a spacecraft at  $\phi$  of  $30^\circ$  will  
 427 detect a 3 decade drop relative to the window center in the power spectral density. Using the  
 428 same assumptions ( $\phi = 0^\circ$ ) as that used in Figure 7 for  $f=53.6$  kHz, we show in Figure 9(d) that

429 inverted-V pattern persists as a function of dB for a plasmopause varying from 1.5 to 4.75 R<sub>E</sub>.  
430 Including attenuation broadens the pattern in  $\theta_B$ . The Budden (1980) formula is valid for any  
431 angle between  $\mathbf{B}$  and  $\nabla Ne$  (gradient of the electron density), except when they are within less  
432 than say 10° of being parallel or anti-parallel. We chose this angle to be 90° (Darrouzet et al.,  
433 2006), therefore the dashed curves shown in the Figure 9(d) we interpreted to be non-valid  
434 solutions of the formula because the incoming wave would be free space instead of Z-mode. If  
435 this interpretation is correct this would also be a factor in contributing to the bias in the  
436 observations having beaming angles above the window center. As the angle between  $\mathbf{B}$  and  $\nabla Ne$   
437 moves away from 90°, more and more of the dashed region becomes valid.

438

439

440 For the NTC beam at 53.6 kHz (Figure 2) the scatter plot of its observed  $\theta_B$  versus time is shown  
441 in Figure 10(a). The black curve is the beaming angle  $\theta_{BC}$  computed from the orbital position  
442 and the equatorial location of the plasmopause (Figure 9b). Based on the earlier discussions it is  
443 not expected that the scatter plot of beaming angle and the beaming angle curve should  
444 quantitatively agree, but they show similar trends with  $\theta_B$  decreasing as the plasmopause is  
445 approached. A scatter plot of its phase space density versus time is shown in Figure 10b. Using  
446  $\theta_{BC}$  the attenuation (blue curve in Figure 10(b)) in dB on transmission through the radio window  
447 is computed using the parameters given in Figure 9(c). The shape of this curve is like the trend in  
448 the scatter, which is level near the window and decreasing moving toward larger radii; however,  
449 the decrease with power and distance from the window is not factored in.

450

451 The solid (dashed) curve is proportional to the product of the radio window attenuation times  
452  $1/\rho_w^2$  ( $1/\rho_w$ ),  $1/\rho_w^2$  would be a point source (Fainberg, J., 1979), and  $1/\rho_w$  would be a line  
453 source. Moving away from the plasmopause the power spectral density decreases by 3 orders of  
454 magnitude. Both the dotted-dashed and dotted curves drop off more rapidly than the observed  
455 scatter. This could be due to at least two factors 1) the true plasmopause of the radio window  
456 location is further outwards in radius than that of the proxy used (Figure 9b). 2) The power  
457 spectral density of the incoming Z mode does not peak at 0 or 180° but peaks at wave normal  
458 angles off 0 or 180°, this would move the  $1/\rho_w^2$  and  $1/\rho_w$  curves to higher PSD moving  
459 outwards in radius. Figure 10(a, b) suggests that a significant fraction of the observations are  
460 emissions that are off centered from the window center.

461

462 For NTC with  $f > 100$  kHz another mechanism along with LMCT must be occurring. At  
463 least three studies have suggested mechanisms for the direct generation of KC. Farrell (2001)  
464 suggested that weak energetic electron beams in a dense warm plasma (where  $f_{pe} \gg f_{ce}$ ) can  
465 directly generate L-O emission with propagation nearly perpendicular. Cheng (1975) has  
466 proposed a mechanism that will lead to near perpendicular beaming using electron ring  
467 distributions as the source. Horky & Omura (2019) performed electromagnetic simulations with  
468 an electron ring beam source in a warm plasma with a density gradient and suggested it can  
469 produce NTC, we believe their figures show near perpendicular beaming. One thing we haven't  
470 addressed is if refraction of the free space for waves with  $f > 100$  kHz, due to density structures  
471 near the radio window, say within a few tens of wavelengths, could focus these waves back  
472 toward the equator. This could be a future study; such a study would also have to explain why  
473 such a mechanism does not occur for the lower frequency waves.

474

475

476 **6 Conclusion**

477         When the Earth's radial vector lay within  $\pm 15^\circ$  of the Van Allen Probes spin plane (in the  
478 dawn sector), spin modulation curve fits were made to the 0.5 s cadence HFR frequency-time  
479 spectra data. These fits were performed at all  $f$  over the entire mission while in the dawn sector,  
480 which covers a vast range of plasmopause locations. To select nonthermal continuum radiation  
481 NTC, frequency-time pixels were selected using the following criteria: the frequency  $f$  was  
482 greater than  $1.2 f_{pe}$ , the modulation index  $m$  was greater than 0.6, the relative error in  $m$  was  
483 small, and the ratio of  $\chi^2/\chi_0^2$  for a sine wave to a constant offset fit was small. A  $m$  of 0.6 was  
484 chosen to ensure that the wave vector  $\mathbf{k}$  lies within  $\sim 30^\circ$  of the spin plane, given the limitation on  
485 the interpretation of  $m$ . The beaming angle  $\theta_B$  was estimated as the angle between the wave  
486 vector direction in the spin plane and the  $Z_{SM}$  axis.

487

488         Below 100 kHz, for a given  $f$  and radial distance bin, the observed pattern of  $\theta_B$  versus  
489 magnetic latitude  $\lambda_M$  forms an inverted-V pattern with the apex at the SM magnetic equator.  
490 Using the NTC beaming formula from LMCT, we show that such a pattern is predicted due to  
491 the large radial variation of the source equatorial plasmopause. Quantitatively the  $\theta_B$  has a  
492 systematic shift above the theory curve near that magnetic equator. A back of the envelope  
493 computation was performed to show that if the plasmopause is not azimuthally symmetric at the  
494 window one expects a systematic offset of  $5\text{-}10^\circ$  toward larger  $\theta_B$ . We discuss several factors  
495 that make the use of  $m$  in estimating the out-of-spin plane component difficult. Two of the  
496 factors are smoothing of data before fitting and variation in the Z-mode intensity at the radio

497 window over the fit interval. By taking attenuation into account (Budden, 1980), we showed that  
498 the model inverted-V becomes broadened in beaming angle by of about  $10^\circ$  near the window  
499 center (Figure 9d) at -20 db. This suggests that attenuation could be the major factor contributing  
500 to the spread in beaming angle. These factors make achievement of quantitative agreement  
501 between observations and theory difficult, if not impossible.

502

503 We found (for  $1 \leq K_p \leq 4$ ) a negative Spearman correlation coefficient for the 3  
504 frequencies investigated below 100 kHz, one with a weak correlation value and two with  
505 moderate values. This trend is expected, because as  $K_p$  index decreases the plasmopause on  
506 average will move outwards and  $f_{ce}$  will decrease leading to a decrease  $\theta_B$  from theory. We  
507 conclude that these two observations, 1) the observed inverted-V pattern of  $\theta_B$  vs  $\lambda_M$  and 2) the  
508 weak to moderate  $K_p$  dependence, highly suggest that LMCT is the dominant mechanism for the  
509 generation of NCT for  $f < 100$  kHz.

510

511 For  $f > 100$  kHz, our selections become contaminated with L-O mode AKR, this contamination  
512 decreases for  $|\lambda_M| (< 10^\circ)$ . A partial inverted-V is observed at the low end of this  $f$  range, and no  
513 reliable trend of  $\theta_B$  with  $K_p$  index is observed. Unlike emissions with  $f < 100$  kHz, where the  
514 clustering of detections tends to lie off the magnetic equator consistent with beaming out the  
515 equatorial plane, in this frequency range these emissions are clustered around the magnetic  
516 equator. We conclude that LMCT can explain only a subset of these observations for  $f > 100$  kHz  
517 and that another mechanism is also needed in this  $f$  range.

518

519 **Acknowledgments**



520 We acknowledge fruitful discussions and comments from Dr. William S. Kurth. The work for  
521 the study was funded by NASA Roses Grant 80HQTR18T0066. This work was also partly  
522 funded by NASA through the GPHI Cooperative Agreement NNG11PL02A and PHASER  
523 80NSSC21M0180. This material is based upon work supported by the U.S. Department of  
524 Energy, Office of Science, Office of Fusion Energy Sciences under contract DE-AC02-  
525 09CH11466. Work at Princeton University is under National Aeronautics and Space  
526 Administration (NASA) Grants 80HQTR18T0066 and 80HQTR19T0076. Work at Andrews  
527 University is supported by NASA grants NNX16AQ87G, 80NSSC19K0270, 80NSSC19K0843,  
528 80NSSC18K0835, 80NSSC20K0355, NNX17AI50G, 80HQTR18T0066, 80NSSC20K0704,  
529 80NSSC18K1578, 80NSSC22K0515, and NSF grants AGS1832207, AGS1602855, and  
530 AGS2131013.

531

### 532 **Data Availability Statement**

533 For attitude calculations, the [NAIF ICY toolkit](#) was used, the ephemeris data required by the  
534 toolkit is at <https://cdaweb.gsfc.nasa.gov/pub/data/rbsp/rbspa/ephemeris/>. The dataset citation for  
535 the HFR spectral data is Kletzing, C. A. (2022a), for plasma density is Kurth et al. (2022), and  
536 the  $K_p$  index is Papitashvili and King, (2020). These datasets are available at the  
537 <https://cdaweb.gsfc.nasa.gov>.)

538

539

### 540 **References**

541 Acton, C.H., Ancillary Data Services of NASA's Navigation and Ancillary Information Facility,  
542 Planetary and Space Science (1996), Vol. 44, No. 1, pp. 65-70;

543 [DOI 10.1016/0032-0633\(95\)00107-7](https://doi.org/10.1016/0032-0633(95)00107-7)

544

545 Acton, C., N. Bachman, B. Semenov, Edward Wright (2017), A look toward the future in the  
546 handling of space science mission geometry; Planetary and Space Science; [DOI](https://doi.org/10.1016/j.pss.2017.02.013)

547 [10.1016/j.pss.2017.02.013](https://doi.org/10.1016/j.pss.2017.02.013)

548

549 Bevington, P.R. & Robinson, D. 1992, *Data Reduction and Error Analysis for the Physical*  
550 *Sciences* (WCB/McGraw-Hill).

551

552 Boardsen, S. A., J. L. Green, and B.W. Reinisch (2008), Comparison of kilometric continuum  
553 latitudinal radiation patterns with linear mode conversion theory, *J. Geophys. Res.*, 113,  
554 A01,219, doi: [10.1029/2007JA012319](https://doi.org/10.1029/2007JA012319).

555

556 Budden, K.G (1980), The theory of radio windows in the ionosphere and magnetosphere,  
557 *Journal of Atmospheric and Terrestrial Physics*, 42-3, [https://doi.org/10.1016/0021-](https://doi.org/10.1016/0021-9169(80)90036-7)

558 [9169\(80\)90036-7](https://doi.org/10.1016/0021-9169(80)90036-7)

559

560 Carpenter, D. L., & Anderson, R. R. (1992). An ISEE/Whistler model of equatorial electron  
561 density in the magnetosphere. *Journal of Geophysical Research*, **97**(A2), 1097– 1108.

562 <https://doi.org/10.1029/91ja01548>

563

564 Cheng, C. -Z. (1975) Ordinary electromagnetic mode instability, *Journal of Plasma Physics*, 13,  
565 pp 335-348, doi [10.1017/S002237780002609X](https://doi.org/10.1017/S002237780002609X)

566

567 Darrouzet, F., De Keyser, J., Decreau, P. M. E., Lemaire, J. F., and Dunlop, M. W. (2006),  
568 Spatial gradients in the plasmasphere from Cluster, *Geophys. Res. Lett.*, 33, L08105,  
569 doi:10.1029/2006GL025727.

570

571 Fainberg, J. (1979), Technique to determine location of radio sources from measurements taken  
572 on spinning spacecraft, NASA Technical Memorandum 80598.

573 <https://ntrs.nasa.gov/citations/19800008000>

574

575 Farrell, W. M. (2001), Direct generation of O-mode emission in a dense, warm plasma:  
576 Applications to interplanetary type II emissions and others in its class, *J. Geophys. Res.*, 106(  
577 A8), 15701– 15709, doi:[10.1029/2000JA000156](https://doi.org/10.1029/2000JA000156).

578

579 Gough, M. P., Christiansen, P., Martelli, G. & Gershuny, E. J. (1979) Interaction of electrostatic  
580 waves with warm electrons at the geomagnetic equator. *Nature* **279**, 515–517,

581 doi:[10.1038/279515a0](https://doi.org/10.1038/279515a0)

582

583 Gough, M.P. (1982) Non-thermal continuum emissions associated with electron injections:  
584 Remote plasmopause sounding, *Planetary and Space Science* **30** (7), 657-668, doi:

585 [https://doi.org/10.1016/0032-0633\(82\)90026-5](https://doi.org/10.1016/0032-0633(82)90026-5).

586

587 Grimald, S., Décréau, P. M. E., Canu, P., Suraud, X., Vallières, X., Darrouzet, F., and Harvey, C.  
588 C. (2007), A quantitative test of Jones NTC beaming theory using CLUSTER constellation, *Ann.*  
589 *Geophys.*, 25, 823–831, doi: [10.5194/angeo-25-823-2007](https://doi.org/10.5194/angeo-25-823-2007).

590

591 Gurnett, D. A. (1975), The Earth as a radio source: The nonthermal continuum, *J. Geophys. Res.*,  
592 80( 19), 2751– 2763, doi:[10.1029/JA080i019p02751](https://doi.org/10.1029/JA080i019p02751).

593

594 Gurnett, D. A., and Green, J. L. (1978), On the polarization and origin of auroral kilometric  
595 radiation, *J. Geophys. Res.*, 83( A2), 689– 696, doi:[10.1029/JA083iA02p00689](https://doi.org/10.1029/JA083iA02p00689).

596

597 Gurnett, D. A., and Frank, L. A. (1976), Continuum radiation associated with low-energy  
598 electrons in the outer radiation zone, *J. Geophys. Res.*, 81( 22), 3875– 3885,  
599 doi:[10.1029/JA081i022p03875](https://doi.org/10.1029/JA081i022p03875).

600

601 Gurnett, D. A., and Shaw, R. R. (1973), Electromagnetic radiation trapped in the magnetosphere  
602 above the plasma frequency, *J. Geophys. Res.*, 78( 34), 8136– 8149,  
603 doi:[10.1029/JA078i034p08136](https://doi.org/10.1029/JA078i034p08136).

604

605 Green, J. L., Gurnett, D. A., and Shawhan, S. D. (1977), The angular distribution of auroral  
606 kilometric radiation, *J. Geophys. Res.*, 82( 13), 1825– 1838, doi:[10.1029/JA082i013p01825](https://doi.org/10.1029/JA082i013p01825).

607

608 Green, J. L., B. Sandel, S. Fung, D. Gallagher, and B. Reinisch (2002), On the origin of  
609 kilometric continuum, *J. Geophys. Res.*, 107, doi: [10.1029/2001JA000193](https://doi.org/10.1029/2001JA000193).

610

611 Green, J. L., Boardsen, S., Fung, S. F., Matsumoto, H., Hashimoto, K., Anderson, R. R., Sandel,  
612 B. R., and Reinisch, B. W. (2004), Association of kilometric continuum radiation with  
613 plasmaspheric structures, *J. Geophys. Res.*, 109, A03203, doi:[10.1029/2003JA010093](https://doi.org/10.1029/2003JA010093).

614

615 Hashimoto, K., Calvert, W., and Matsumoto, H. (1999), Kilometric continuum detected by  
616 Geotail, *J. Geophys. Res.*, 104( A12), 28645– 28656, doi:[10.1029/1999JA900365](https://doi.org/10.1029/1999JA900365).

617

618 Hashimoto, K., Anderson, R. R., Green, J. L., and Matsumoto, H. (2005), Source and  
619 propagation characteristics of kilometric continuum observed with multiple satellites, *J.*  
620 *Geophys. Res.*, 110, A09229, doi:[10.1029/2004JA010729](https://doi.org/10.1029/2004JA010729).

621

622 Horkey, M. and Y. Omura (2019), Novel nonlinear mechanism of the generation of non-thermal  
623 continuum radiation, *Physics of Plasmas* **26**, 022904 (2019); <https://doi.org/10.1063/1.5077094>

624

625 Horne, R. B. (1989), Path-integrated growth of electrostatic waves: The generation of terrestrial  
626 myriametric radiation, *J. Geophys. Res.*, 94( A7), 8895– 8909, doi:[10.1029/JA094iA07p08895](https://doi.org/10.1029/JA094iA07p08895).

627

628 Jones, D. (1976), Source of terrestrial non-thermal radiation *Nature* **260**, 686–689,

629 <https://doi.org/10.1038/260686a0>

630

631 Jones, D. (1980), Latitudinal beaming of planetary radio emissions. *Nature* **288**, 225–229.

632 <https://doi.org/10.1038/288225a0>

633

634 Jones, D., Calvert, W., Gurnett, D. A., & Huff, R. L. (1987), Observed beaming of terrestrial  
635 myriametric radiation. *Nature* **328**, 391–395. <https://doi.org/10.1038/328391a0>

636

637 Kim, E.-H., I. H. Cairns, and J. R. Johnson (2013), Linear mode conversion of Langmuir/z-mode  
638 waves to radiation in various magnetic field strength plasmas, *Physics of Plasmas*, 20, 122103.  
639 <https://doi.org/10.1063/1.4837515>

640

641 Kletzing, C. A., et al. (2013), The Electric and Magnetic Field Instrument Suite and Integrated  
642 Science (EMFISIS) on RBSP, *Space Sci. Rev.*, 179, 127–181, doi:[10.1007/s11214-013-9993-6](https://doi.org/10.1007/s11214-013-9993-6).

643

644 Kletzing, C. A. (2022), Van Allen Probe A Single Axis AC Electric Field Spectra burst data  
645 [Data set]. NASA Space Physics Data Facility. <https://doi.org/10.48322/18b2-kt74>.

646

647 Kurth, W.S. (1982), Detailed observations of the source of terrestrial narrowband  
648 electromagnetic radiation. *Geophys. Res. Lett.*, 9: 1341-1344.  
649 <https://doi.org/10.1029/GL009i012p01341>

650

651 Kurth, W. S., Baumbach, M. M., and Gurnett, D. A. (1975), Direction-finding measurements of  
652 auroral kilometric radiation, *J. Geophys. Res.*, 80( 19), 2764– 2770,  
653 doi:[10.1029/JA080i019p02764](https://doi.org/10.1029/JA080i019p02764).

654

655 Kurth, W.S., Frank, L.A., Ashour-Abdalla, M., Gurnett, D.A. and Burek, B.G. (1980),  
656 Observations of a free-energy source for intense electrostatic waves. *Geophys. Res. Lett.*, 7: 293-  
657 296. <https://doi.org/10.1029/GL007i005p00293>

658

659 Kurth, W. S., Gurnett, D. A., and Anderson, R. R. (1981), Escaping nonthermal continuum  
660 radiation, *J. Geophys. Res.*, 86( A7), 5519– 5531, doi:[10.1029/JA086iA07p05519](https://doi.org/10.1029/JA086iA07p05519).

661

662 Kurth, W. S., De Pascuale, S., Faden, J. B., Kletzing, C. A., Hospodarsky, G. B., Thaller, S. and  
663 Wygant, J. R. (2015), Electron densities inferred from plasma wave spectra obtained by the  
664 Waves instrument on Van Allen Probes. *J. Geophys. Res. Space Physics*, 120: 904– 914. doi:  
665 [10.1002/2014JA020857](https://doi.org/10.1002/2014JA020857).

666

667 Kurth, W. S., S. De Pascuale, J. B. Faden, C. A. Kletzing, G. B. Hospodarsky, S. Thaller, and J.  
668 R. Wygant (2022). Van Allen Probe A Electric and Magnetic Field Instrument Suite and  
669 Integrated Science (EMFISIS) Density and other Parameters derived by digitizing Traces on  
670 Spectrograms, Level 4 (L4), 0.5 s Data [Data set]: RBSP-A\_DENSITY\_EMFISIS-L4. NASA  
671 Space Physics Data Facility. <https://doi.org/10.48322/c4ha-xj50>.

672

673 Menietti, J. D., Gurnett, D. A., Kurth, W. S., Groene, J. B., and Granroth, L. J. (1998), Galileo  
674 direction finding of Jovian radio emissions, *J. Geophys. Res.*, 103( E9), 20001– 20010,  
675 doi:[10.1029/97JE03555](https://doi.org/10.1029/97JE03555).

676

677 Moldwin, M. B., Downward, L., Rassoul, H. K., Amin, R., & Anderson, R. R. (2002). A new  
678 model of the location of the plasmapause: CRRES results. *Journal of Geophysical Research*,  
679 **107**(A11). SMP1-9–SMP2-9. <https://doi.org/10.1029/2001ja009211>

680

681 Morgan, D. D., and D. A. Gurnett (1991), The source location and beaming of terrestrial  
682 continuum radiation, *J. Geophys. Res.*, 96, 9595. <https://doi.org/10.1029/91JA00314>

683

684 Papitashvili, N. E., & and King, J. H. (2020), OMNI Hourly Data Set [Data set]. NASA Space  
685 Physics Data Facility. <https://doi.org/10.48322/1shr-ht18>.

686

687

688 Rönmark, K., Christiansen, P. Dayside electron cyclotron harmonic emissions.  
689 *Nature* **294**, 335–338 (1981). <https://doi.org/10.1038/294335a0>

690

691 Sandel, B., Goldstein, J., Gallagher, D. *et al.* Extreme Ultraviolet Imager Observations of the  
692 Structure and Dynamics of the Plasmasphere. *Space Science Reviews* **109**, 25–46 (2003).  
693 <https://doi.org/10.1023/B:SPAC.0000007511.47727.5b>

694

695 Schleyer, F., I. H. Cairns, and E.-H. Kim (2014), Linear mode conversion of upper hybrid waves  
696 to radiation: Averaged energy conversion efficiencies, polarization, and applications to Earth's  
697 magnetosphere, *J. Geophys. Res.* 119, 3392–3410, doi:10.1002/2013JA019364.

698



699 Sentman, D.D., Frank, L.A., Gurnett, D.A., Kurth, W.S. and Kennel, C.F. (1979), Electron  
 700 distribution functions associated with electrostatic emissions in the dayside magnetosphere.

701 *Geophys. Res. Lett.*, 6: 781-784. <https://doi.org/10.1029/GL006i010p00781>

702

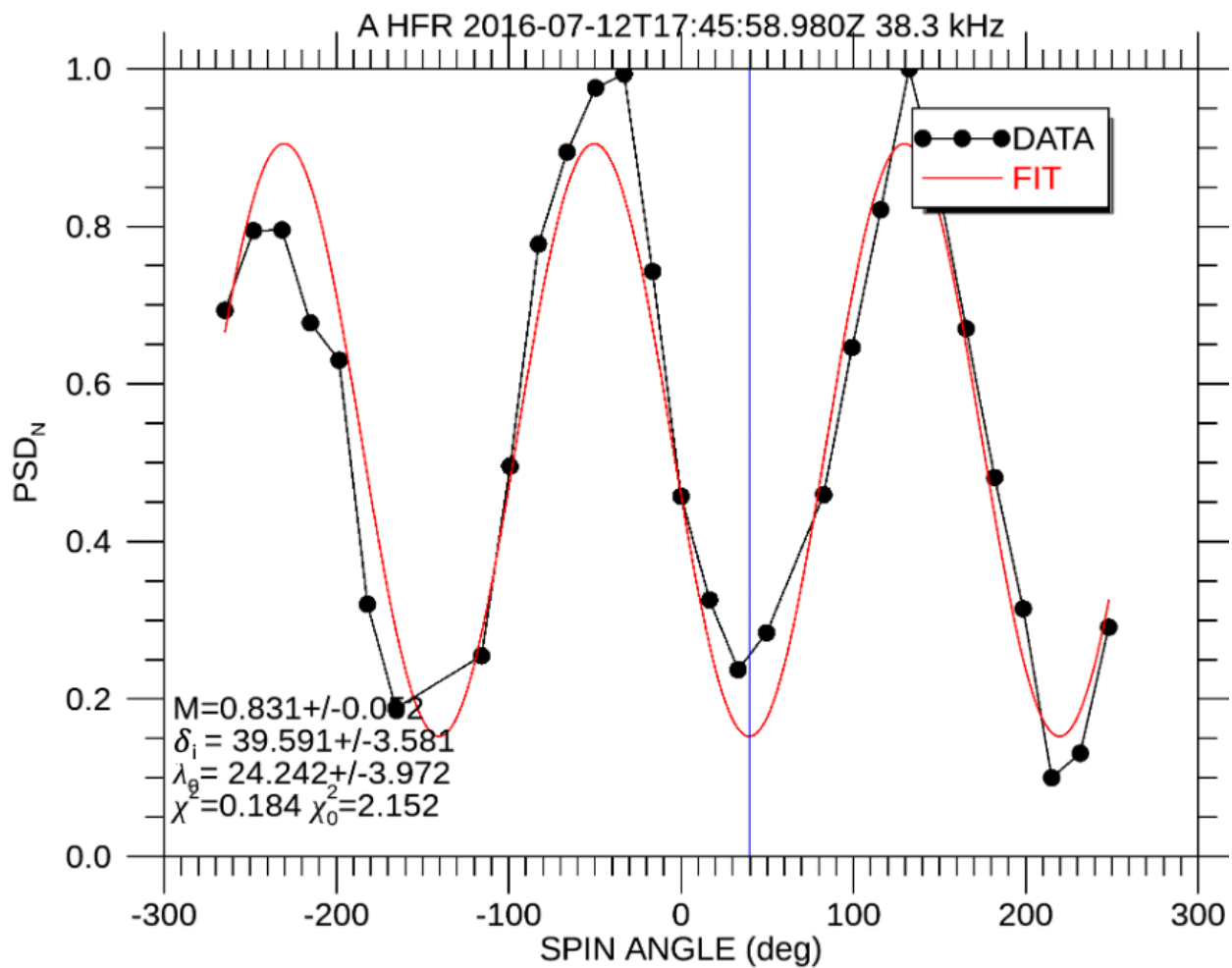
703 Xiao, F., Zhou, Q., Su, Z., He, Z., Yang, C., Liu, S., He, Y., and Gao, Z. (2016), Explaining

704 occurrences of auroral kilometric radiation in Van Allen radiation belts, *Geophys. Res. Lett.*, 43,

705 11,971– 11,978, doi:[10.1002/2016GL071728](https://doi.org/10.1002/2016GL071728).

706

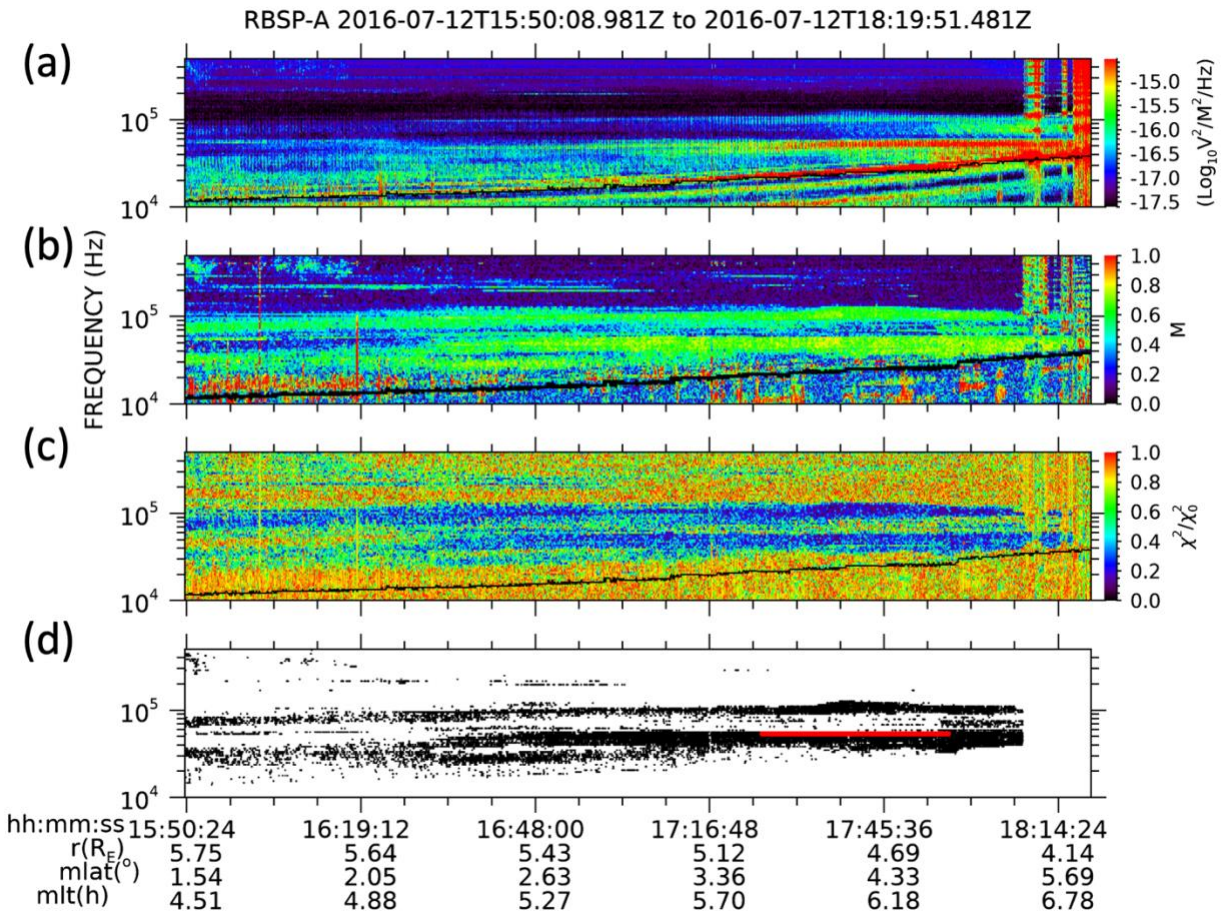
707



708

709 Figure 1. An example fit of the spin modulation curve for the frequency channel at 38.3 kHz.  
710 The fit parameters and their uncertainties are listed. The power spectral density  $\text{PSD}_N$  is  
711 normalized to the peak value.  $\chi^2$  is the chi squared of the spin modulation curve fit and  $\chi^2_0$  is the  
712 chi squared for a constant offset fit.  
713

714

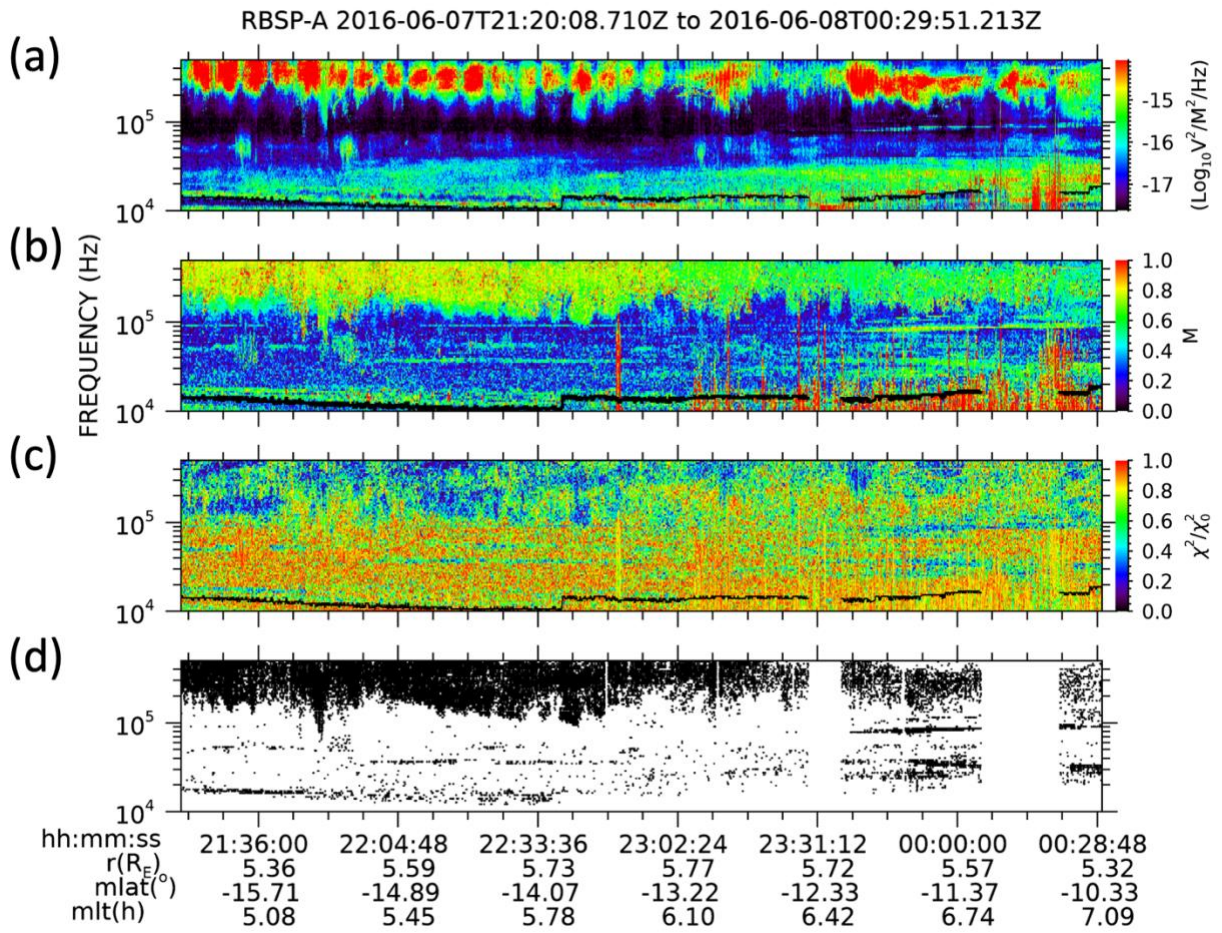


715

716 Figure 2. Escaping continuum example. Panel (a) spectrogram of the phase space density, (b)  
 717 spectrogram of the modulation index  $m$ , (c)  $\chi^2/\chi^2_0$  ratio, and (d) selections. The black line is the  
 718 UHF derived plasma frequency. The red lines in panel (d) correspond to selections at 53.6 kHz  
 719 between 4.5 and 5  $R_E$  used in Figure 8, 9 & 10.

720

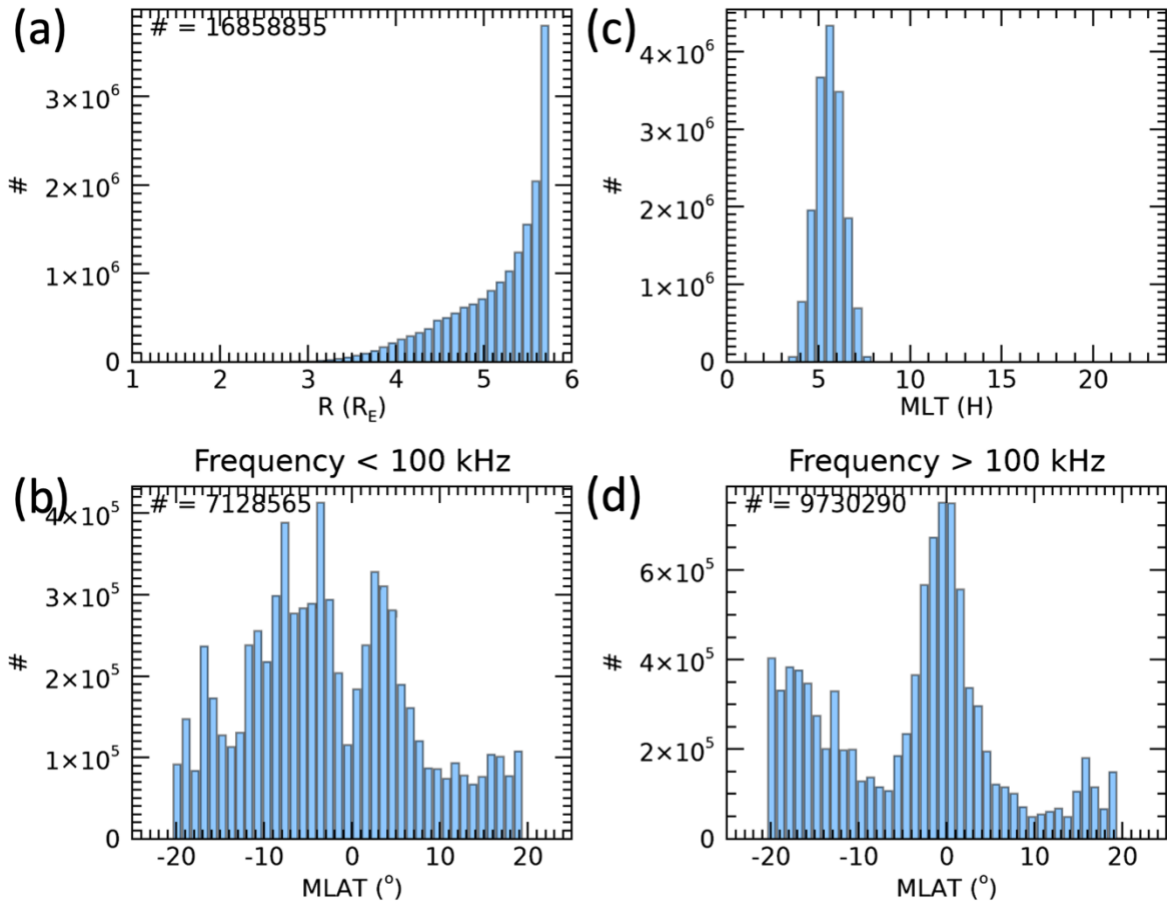
721



722

723 Figure 3. Emissions at  $f$  from 200 to 500 kHz are interpreted to be L-O mode AKR a source of  
 724 contamination of the selections above 100 kHz. Panel (a) spectrogram of the phase space density,  
 725 (b) spectrogram of the modulation index  $m$ , (c)  $\chi^2/\chi_0^2$  ratio, and (d) selections. The black line is  
 726 the UHF derived plasma frequency.

727



728

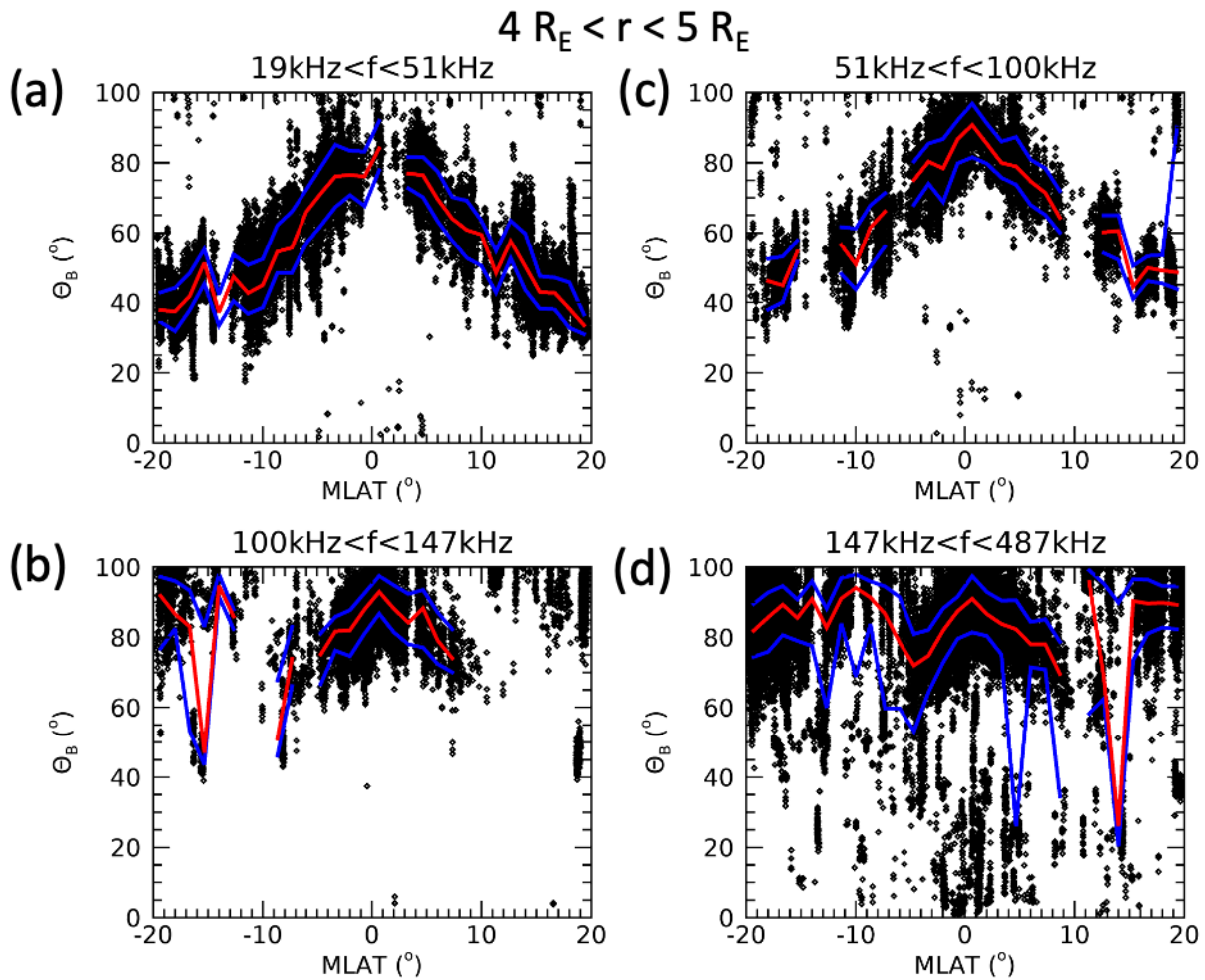
729 Figure 4. Histogram of the selections: (a) radial distance, (b) magnetic latitude for  $f < 100$  kHz,

730 (c) magnetic local time, and (d) magnetic latitude for  $f > 100$  kHz.

731



732

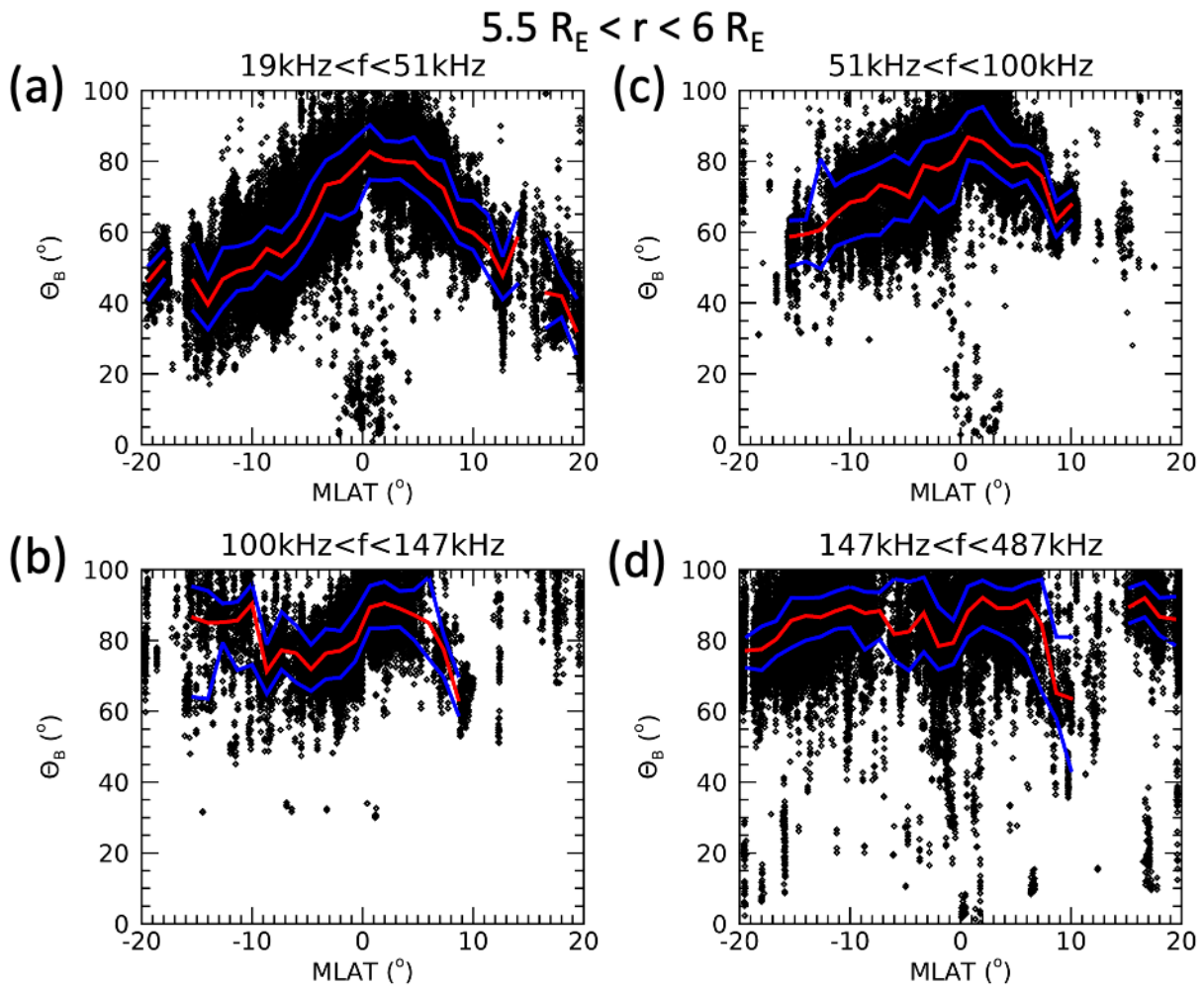


733

734 Figure 5. Scatter plots for  $4 R_E < r < 5 R_E$  of beaming angle  $\theta_B$  versus magnetic latitude. For (a)  $f$ 735  $< 50$  kHz, (b)  $50\text{kHz} < f < 100\text{kHz}$ , (c)  $100\text{kHz} < f < 150\text{kHz}$ , and (d)  $150\text{kHz} < f < 500\text{kHz}$ . The736 curves are the running percentiles, red 50<sup>th</sup> (median), blue 16<sup>th</sup> and 84<sup>th</sup> percentiles.

737

738

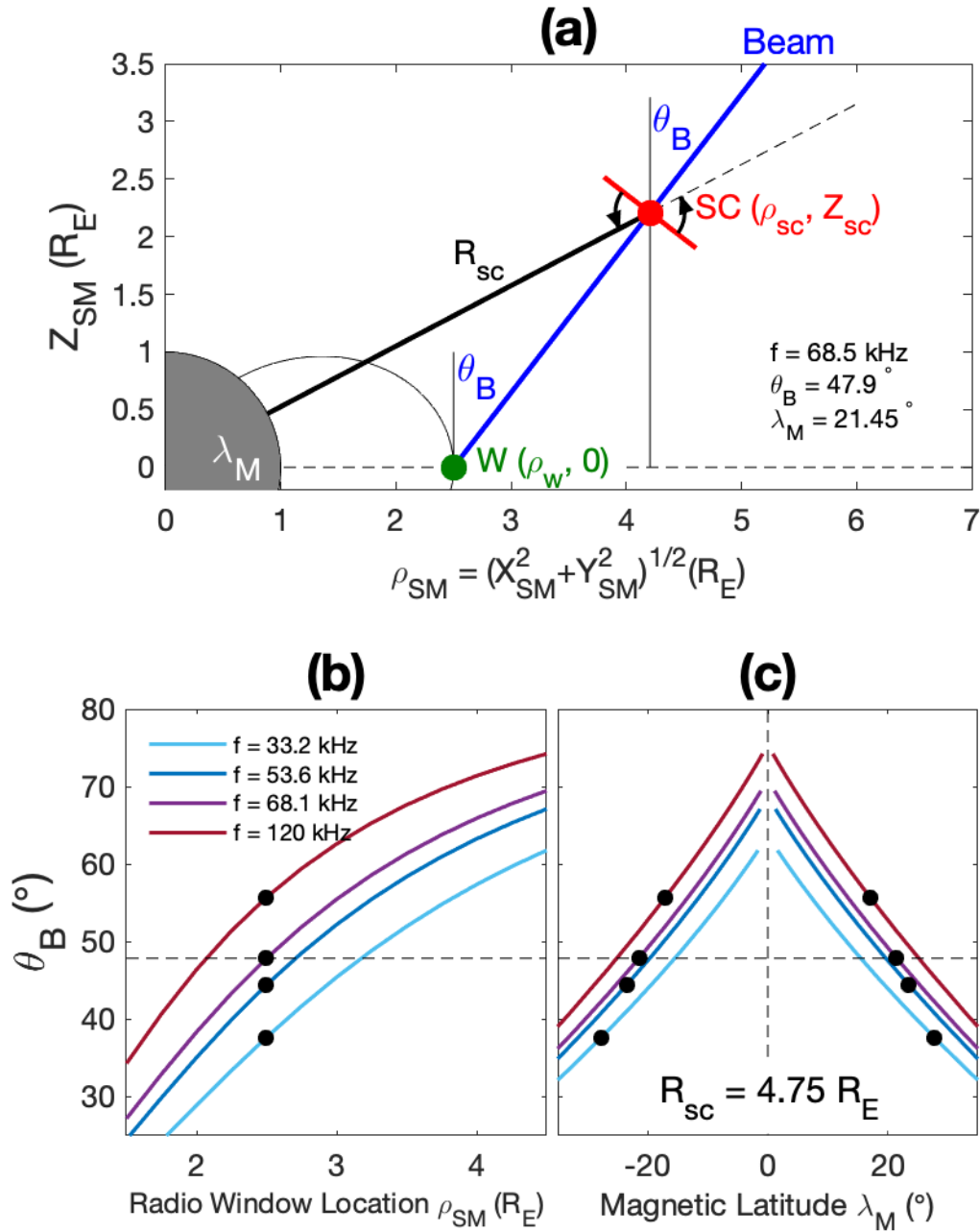


739

740 Figure 6. Scatter plots for  $r > 5.5 R_E$  of beaming angle  $\theta_B$  versus magnetic latitude. For (a)  $f < 50$ 741 kHz, (b)  $50\text{kHz} < f < 100\text{kHz}$ , (c)  $100\text{kHz} < f < 150\text{kHz}$ , and (d)  $150\text{kHz} < f < 500\text{kHz}$ . The742 curves are the running percentiles, red 50<sup>th</sup> (median), blue 16<sup>th</sup> and 84<sup>th</sup> percentiles.

743

744



745

746 Figure 7 (a) Illustration of the meridian beaming geometry. The blue line represents the NTC  
 747 beam emitted at the radio window  $W$  (green circle). The satellite  $SC$  (red circle) is at a radial  
 748 distance  $R_{sc}$  and magnetic latitude  $\lambda_M$ .  $\theta_B$  is measured from background magnetic field  $\mathbf{B}$  ( $\mathbf{B} \parallel$

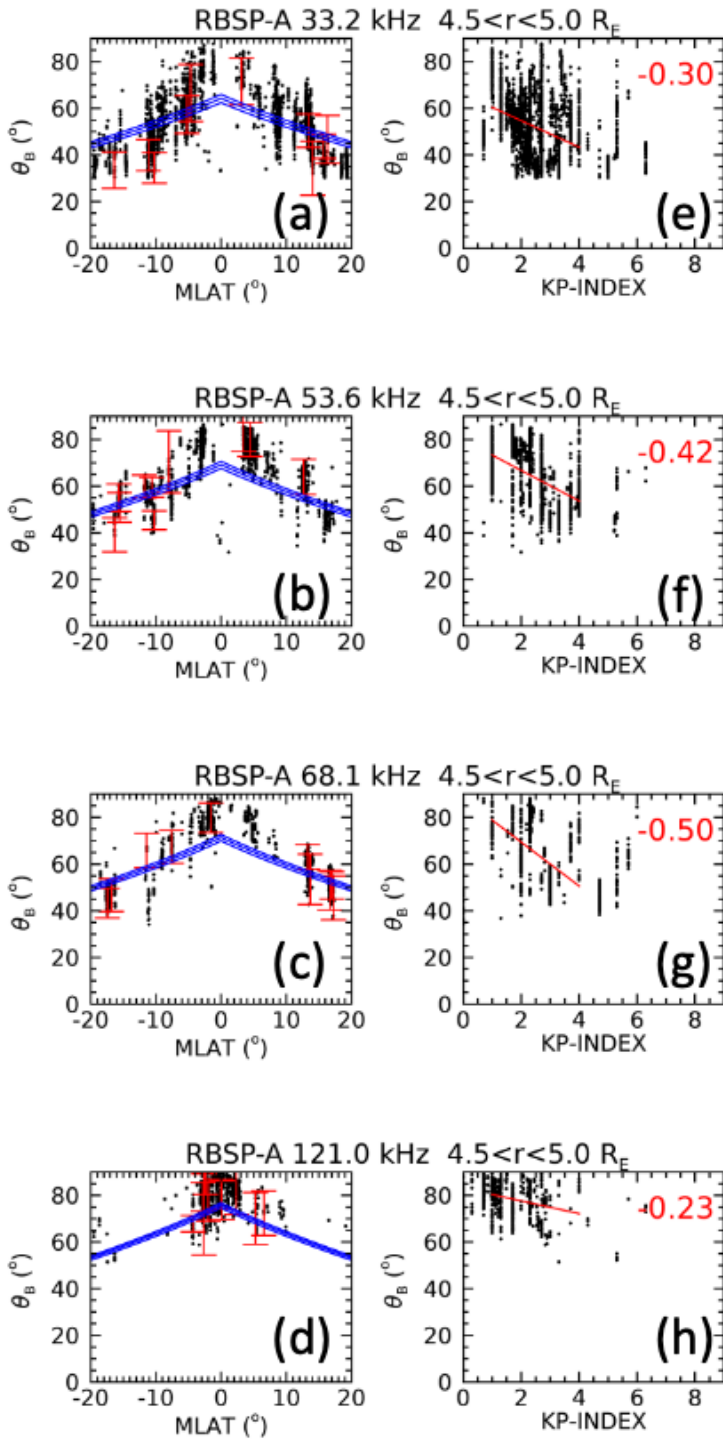
749  $\mathbf{Z}_{SM}$ ) at  $W$ . (b)  $\theta_B$  as  $W$  changes with radial distance.  $\theta_B$  (black circles) when  $W$  is located at

750  $L=2.5R_E$  (i.e., the plasmopause is at  $2.5R_E$ ). (c) The predicted  $\theta_B$  for  $R_{sc}$  at  $4.75 R_E$  versus  $\lambda_M$  for



751 plasmopause locations varying between 1.5 to 4.75  $R_E$ . For example, at  $f = 68.1$  kHz emission  
752 from a plasmopause located at  $2.5R_E$  with a  $\theta_B$  of  $47.9^\circ$  (b) will be observed by a spacecraft at  
753  $4.75R_E$  at  $\lambda_M$  of  $\pm 21.45^\circ$ , indicated by the dashed horizontal line in panels (b) and (c).

754



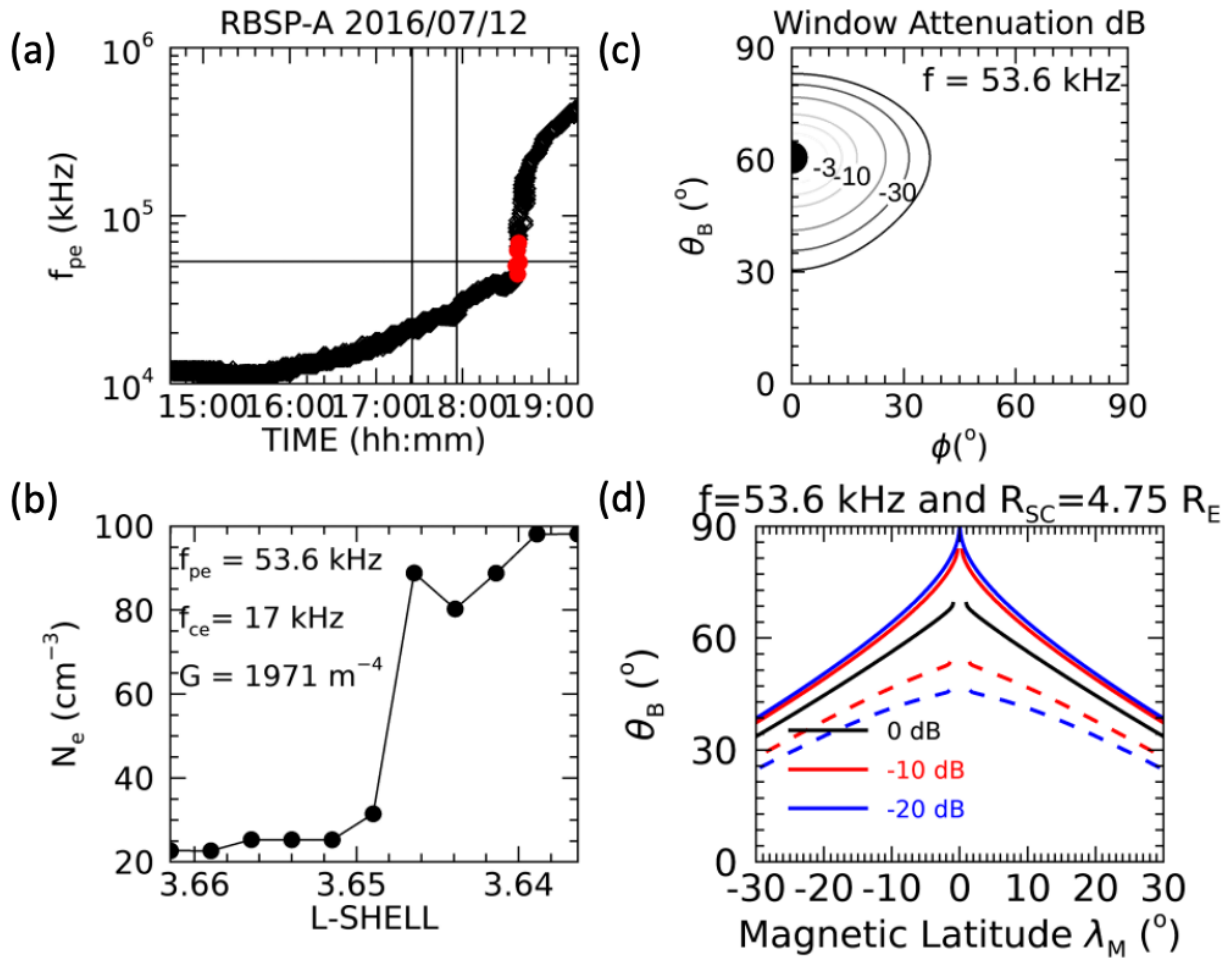
755

756 Figure 8. Scatter plots for  $r$  between 4.5 and 5.0  $R_E$ ; beaming angle (a-d)  $\theta_B$  versus magnetic

757 latitude and (e-i)  $K_p$  index, for frequencies of 33.2 kHz, 53.6 kHz, 68.1 kHz, and 121.0 kHz. The

758 blue curves (a-d) are the statistical LMCT theory curves for  $r$  of 4.5, 4.75, and 5.0  $R_E$ . Error bars  
759 indicated by red brackets are plotted for 10 randomly selected measurements. In (e-h) the red  
760 lines are linear fits, and the red numbers are the non-linear Spearman correlation coefficients,  
761 which lie in the (e) weak, (f) moderate, (g) moderate, and (h) poor range.  
762

763



764

765 Figure 9 (a) The nearest plasmopause is indicated (red dots), where  $f = 53.6$  kHz intersects  $f_{pe}$  for

766 the NTC emissions shown in Figure 2. The vertical lines are where the orbit goes from 5.0 to 4.5

767 RE. (b) The intersection point is at  $L=3.65$ , magnetic latitude =  $7.18^\circ$ ,  $MLT=7$  h, the radial

768 electron density gradient is  $G$  is  $-1971 \text{ m}^{-4}$ . (c) For  $f=53.6$  kHz the radio window attenuation in

769 decibels is shown as a function  $\theta_B$  and  $\phi$  (azimuthal angle measured from the plasmopause).

770 The window center is indicated by the black dot where the attenuation is 0 dB (100%

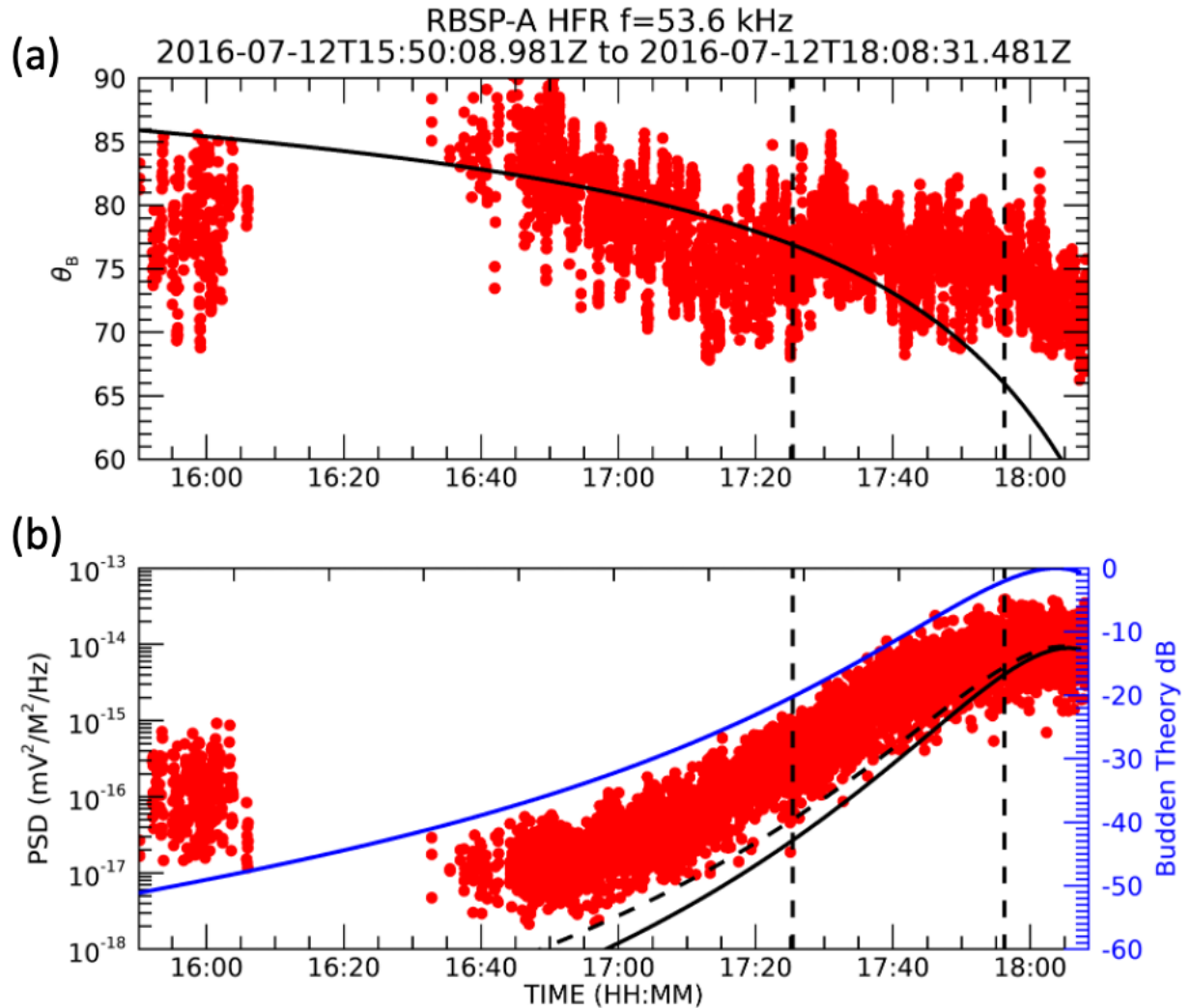
771 transmission). (d) The inverted-V pattern is shown for  $f = 53.6$  kHz using same assumptions as in

772 Figure 7, but attenuation of emissions that are off centered are included. Black curve is at the

773 window center, same as that of Figure 7, the red (blue) curves are for emissions attenuated by -  
774 10 dB (-20 dB). The dashed curves are interpreted to be non-physical solutions (see text).

775

776



777

778 Figure 10. At a frequency of 53.6 kHz for the orbit segment shown in Figure 2 a scatter plot (red

779 circles) is shown of (a) signal measured  $\theta_B$  and (b) Power Spectral Density versus time. The780 black curve in (a) is  $\theta_B$  based on the spacecraft location and the estimated window location, and

781 the blue curve for (b) is the attenuation of the signal in decibels given by equation (23) of

782 Budden (1980) (right y-axis) for the curve in (a). The dashed and dotted lines are the PSD

783 proportional to the power of the attenuation times  $1/\rho_w^2$  and  $1/\rho_w$  respectively. The two vertical784 dashed lines are where the orbit goes from 5.0 to 4.5  $R_E$ .

785